

Chapter 2

Experiment

One of Europe’s first joint ventures in science [82], CERN (*Conseil Européen pour la Recherche Nucléaire*) is the largest physics research facility in the world, bringing together more than 12,400 scientists of over 110 nationalities [83] with a common goal of pushing the frontiers of science and technology. Located at the Franco–Swiss border near Geneva, CERN was founded in 1954 and nowadays counts 23 member states [83]. CERN’s main research area is particle physics, hence why the organisation operates a large complex of particle accelerators and detectors.

This chapter introduces the Large Hadron Collider (LHC), CERN’s main particle accelerator, as well as the ATLAS experiment, in which the search for Supersymmetry (SUSY) presented in this work is embedded in.

2.1 The Large Hadron Collider

The LHC [84] is the largest particle accelerator situated at CERN. It is installed in a tunnel with 26.7 km circumference, that was originally constructed from 1984 to 1989 for the Large Electron Positron (LEP) accelerator. The tunnel is situated on the Franco–Swiss border and wedged between the Jura mountains and lake Léman. It lies between 45 m (in the limestone of the Jura) and 170 m (in the molasse rock) below the surface, resulting in a tilt of 1.4% towards the lake. While proton–proton (pp) collisions are the main operating mode of the LHC, its design also allows it to accelerate and collide heavy ions like lead and xenon. Since data from pp collisions is used in this work, the following sections will mainly focus on this operating mode. As opposed to particle–antiparticle colliders that only need a single ring, the LHC, being a particle–particle collider, consists of two rings with counter-rotating beams. With an inner diameter of only 3.7 m, the tunnel is however simply too narrow to fit two separate proton rings. Instead, the LHC is built in a twin bore design[†], housing two sets of coils and beam channels in a single magnetic and mechanical structure and cryostat [84]. While saving costs, this design has the disadvantage of both beams being magnetically coupled, consequently reducing the flexibility of the machine.

[†] Originally proposed by John Blewett at BNL for cost-saving measures of the Colliding Beam Accelerator [85, 86].

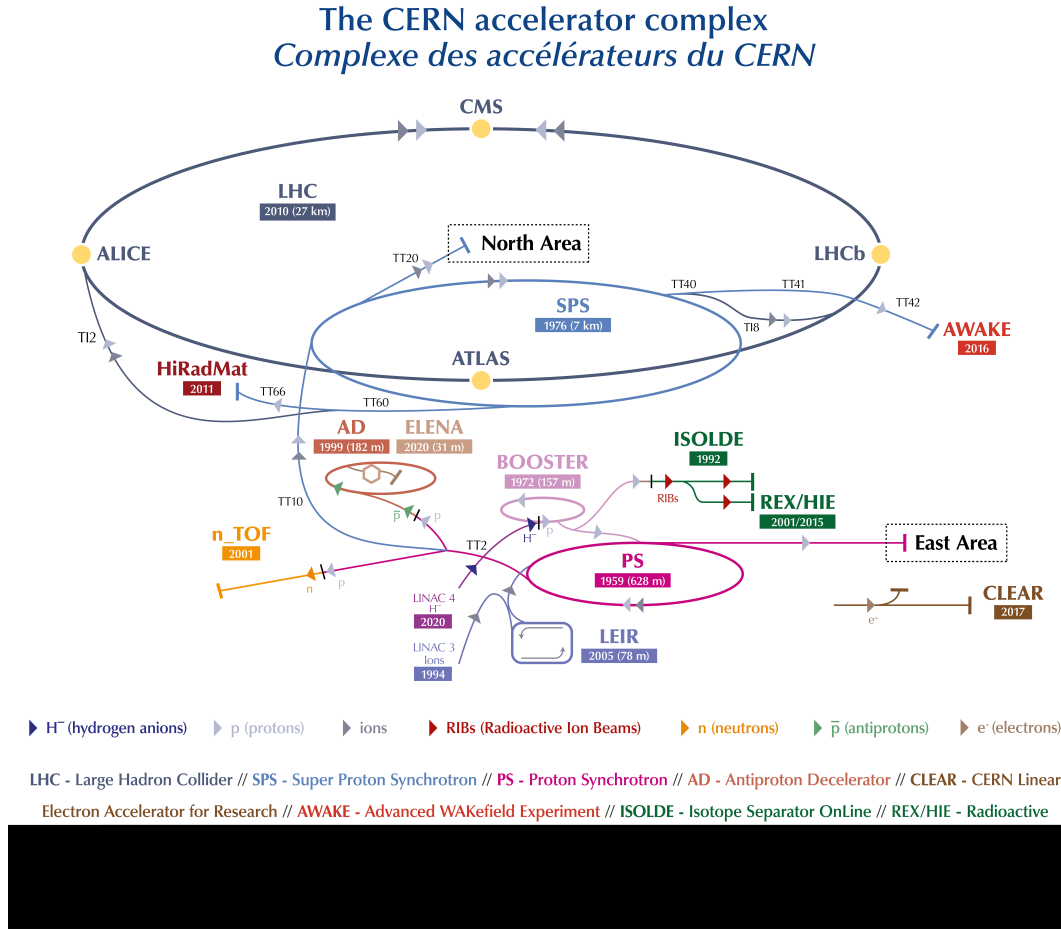


Figure 2.1: CERN accelerator complex as of 2021 [89].

Before being injected into the LHC, protons are pre-accelerated in an injection chain consisting of multiple existing machines in CERN's accelerator complex, pictured in fig. 2.1. The injection chain uses predecessor accelerators that have been upgraded in order to be able to handle the high luminosity and high energy requirements of the LHC. The protons for the LHC originally stem from a duoplasmatron source [87], stripping electrons from hydrogen atoms through electric discharges between a hot anode and cathode. The 90 keV protons are then accelerated by a radio frequency (RF) quadrupole to 750 keV before being injected into Linac 2[†], a linear accelerator producing a beam of 50 MeV protons through the use of RF cavities. The protons then enter a set of circular accelerators, the Proton Synchrotron Booster, the Proton Synchrotron and the Super Proton Synchrotron, creating a stepwise acceleration up to an energy of 450 GeV, which is the injection energy of the LHC. The LHC finally accelerates the protons up to nominal beam energy before colliding them.

The LHC is composed of eight straight sections and eight arcs. The eight straight sections each serve as interaction points (referred to as *Point* in the following), either for particle detectors,

[†] Originally built to replace Linac 1 in order to produce higher energetic proton beams, Linac 2 has been replaced by Linac 4 in 2020 [88]. Linac 3 was built in 1994 and is still used for acceleration of heavy ions.

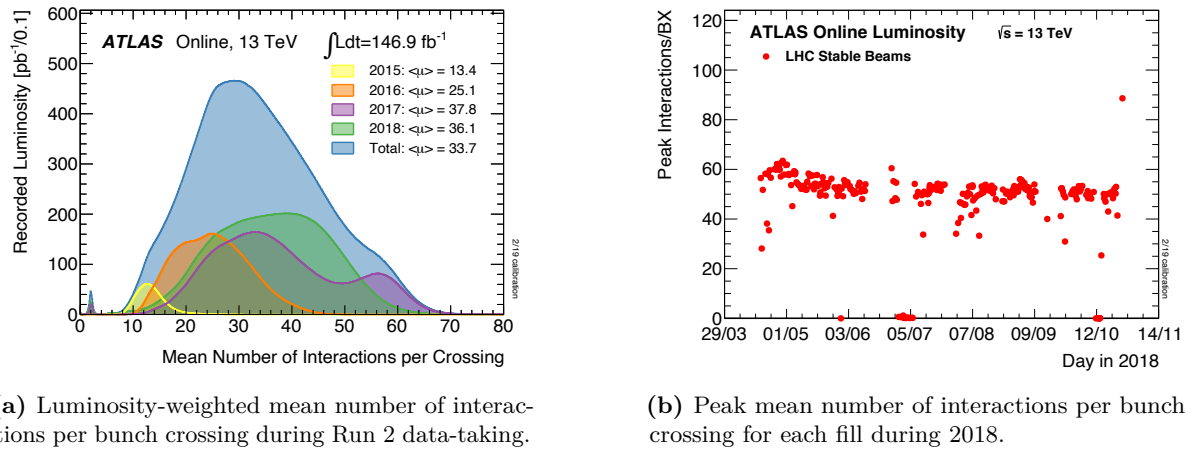
or for machine hardware of the collider itself. The Points are labelled clockwise, with Point 1 being closest to the CERN Meyrin site. Four of the eight Points house the main particle physics experiments at the LHC, called ATLAS, CMS, ALICE and LHCb, covering a wide range of fundamental research. The two general purpose particle detectors ATLAS [90] and CMS [91] are installed at Point 1 and Point 5, respectively. Both ATLAS and CMS are designed to perform high precision SM measurements including Higgs measurements as well as searches for BSM physics. Being very similar in terms of targeted phase space, ATLAS and CMS can be used to cross-check results of each other. ALICE [92] is situated at Point 2 and specializes on heavy ion physics, studying the physics of quark-gluon plasma at high energy densities. Assembled in Point 8, LHCb [93] targets B -physics and performs measurements of CP-violation. Apart from the four main experiments, three smaller experiments exist at the LHC: TOTEM, MoEDAL and LHCf. While TOTEM [94] and LHCf [95] study forwards physics close to CMS and ATLAS, respectively, MoEDAL [96] searches for magnetic monopoles.

The remaining four Points house accelerator equipment needed for operation of the LHC. Most of the collimation system is placed at Point 3 and Point 7, performing beam cleaning and machine protection through a series of beam intercepting devices, ensuring that no stray particles from experimental debris or beam halo can reach and damage other machine components [84]. The acceleration of the beam itself is performed at Point 4 with two RF systems, one for each LHC beam. The RF cavities operate at 400 MHz and provide 8 MV during injection and 16 MV during coast [84]. Due to the RF acceleration, the accelerated protons are necessarily grouped in packages called *bunches*, each containing roughly 10^{11} protons, with a bunch spacing of 25 ns [84]. Although roughly 35,500 RF buckets are available, a design-value of only 2808 bunches are filled in each beam for data-handling reasons [84]. The remaining Point 6 houses the beam dumping system, allowing to horizontally deflect and fan out both beams into dump absorbers using fast-paced *kicker* magnets. The two nitrogen-cooled dump absorbers each consist of a graphite core contained in a steel cylinder, surrounded by 750 t [84] of concrete and iron shielding. Insertion of the beams from the Super Proton Synchrotron into the LHC happens at Points 2 and 8, close to the ALICE and LHCb experiments.

The eight arcs of the LHC are filled with dipole magnets built from superconducting NbTi Rutherford cables. The electromagnets are responsible for keeping the accelerated particles on their circular trajectory and are the limiting factor of the maximal centre-of-mass energy, \sqrt{s} , of the LHC. In order to achieve the design energy of $\sqrt{s} = 14$ TeV [84], the magnets have to create a field strength of 8.3 T [84]. In order to sustain the electric currents needed for such high field strengths, the magnets need to be cooled down to 1.9 K [84] using superfluid helium and operated in superconducting state. In addition to the dipole magnets, the arcs contain quadrupole magnets used to shape and focus the beams, as well as multipole magnets correcting and optimising the beam trajectory. Quadrupole magnets are also used to reduce the beam size before and after the interaction points.

2.1.1 Pile-up

Due to the high number of protons in each bunch, several pp collisions occur at each bunch crossing. This leads to a phenomenon called *pile-up*, where the recorded events not only contain information from the hard-scattering process of interest, but also remnants from additional, often low-energy, pp collisions. During the Run 2 data-taking period, i.e. the period from 2015



(a) Luminosity-weighted mean number of interactions per bunch crossing during Run 2 data-taking.

(b) Peak mean number of interactions per bunch crossing for each fill during 2018.

Figure 2.2: Number of interactions per bunch crossing recorded by the ATLAS experiment [97].

throughout 2018, the mean number of inelastic pp collisions per bunch crossing, μ , has varied from roughly from 10 to 70, with the majority of bunch crossings having a value of μ around 30. Figure 2.2(a) shows the mean number of interactions per bunch crossing during the Run 2 data-taking period, weighted by luminosity (a quantity introduced in section 2.1.2). The peak number of interactions per bunch crossing, μ_{peak} , has been consistently around 50 during the 2018 data-taking for each fill (cf. fig. 2.2(b)).

Experimentally, pile-up can be divided into five major components [98]:

- *In-time* pile-up: multiple interactions during a single bunch crossing, of which not all will be interesting, as often with relatively low energy. If they can be resolved, the main hard-scattering event can still be isolated and studied.
- *Out-of-time* pile-up: additional collisions occurring in bunch crossings before or after the main event of interest. This happens either due to read-out electronics integrating over longer time frames than the 25 ns bunch spacing, or detector components being sensitive to several bunch crossings.
- *Cavern background*: gas of thermal neutrons and photons that fill the experimental caverns during a run of the LHC and tend to cause random hits in detector components.
- *Beam halo events*: protons scraping an up-stream collimator, typically resulting in muons travelling parallel to the beam pipe.
- *Beam gas events*: interactions between proton bunches and residual gas in the beam pipe.

While the effects of cavern background can be mitigated through special pieces of shielding, beam halo and beam gas events leave signatures that can be recognised and removed. Signals from in-time and out-of-time pile-up create irreducible overlap with the events of interest, significantly impacting analyses, and thus need to be simulated [98].

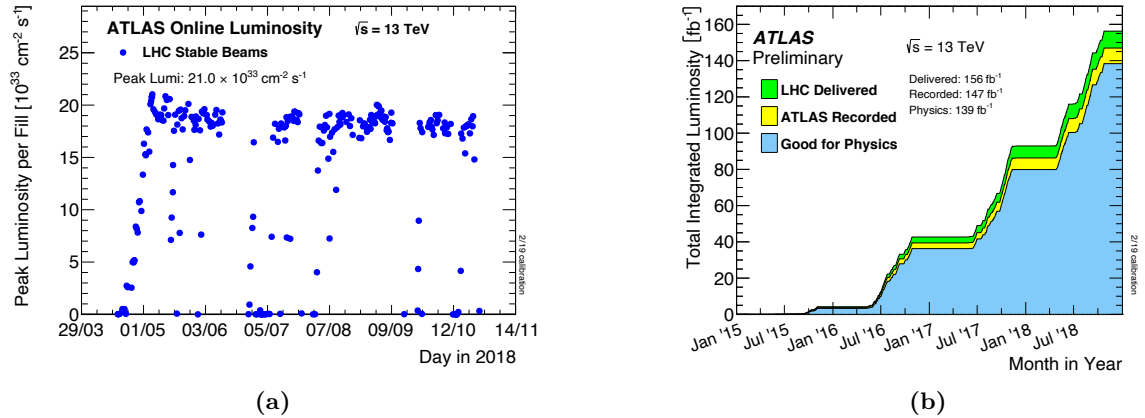


Figure 2.3: Instantaneous and cumulative luminosities in Run 2. Figure (a) shows the peak instantaneous luminosity delivered to ATLAS during pp collision data taking in 2018 as a function of time. Figure (b) shows the cumulative luminosity delivered to ATLAS (green), recorded by ATLAS (yellow) and deemed good for physics analysis (blue) during the entirety of Run 2 [97].

2.1.2 Luminosity and data-taking

Apart from the beam energy, the most important quantity for a collider is the instantaneous luminosity L_{inst} . For a synchrotron with Gaussian beam distribution, the instantaneous luminosity can be written as

$$L_{\text{inst}} = \frac{N_b^2 n_b f_{\text{rev}}}{4\pi\sigma_x\sigma_y} F, \quad (2.1)$$

where n_b is the number of bunches, N_b the number of protons per bunch, f_{rev} the revolution frequency and σ_x and σ_y the transverse beam sizes. The parameter F is a geometrical correction factor accounting for the reduction in instantaneous luminosity due to the beams crossing at a certain crossing angle. While the design instantaneous luminosity of the LHC at the high-luminosity experiments ATLAS and CMS is $L_{\text{inst}} = 10^{34} \text{ cm}^{-2} \text{ s}^{-1}$ [84], the 2017 and 2018 data-taking periods saw a peak luminosity twice as high [99].

The instantaneous luminosity is related to the total number of events N through the cross section σ of the events in question

$$N = \sigma L = \sigma \int L_{\text{inst}} dt, \quad (2.2)$$

with L the total integrated luminosity, a measure for the total amount of collision data produced.

A precise knowledge of the integrated luminosity corresponding to a given dataset is crucial for both SM measurements as well as searches for beyond the Standard Model (BSM) physics. Searches for SUSY like the one presented in this work rely on precise measurements of the integrated luminosity in order to be able to estimate the contribution from SM background processes. The luminosity measurement for the Run 2 dataset used within this work is described in detail in Refs. [100, 101] and relies on a measurement of the bunch luminosity L_b , i.e. the

luminosity produced by a single pair of colliding bunches,

$$L_b = \frac{\mu f_{\text{rev}}}{\sigma_{\text{inel}}} = \frac{\mu_{\text{vis}} f_{\text{rev}}}{\sigma_{\text{vis}}}, \quad (2.3)$$

with μ the pile-up parameter, σ_{inel} the cross section of inelastic pp collisions, $\mu_{\text{vis}} = \epsilon\mu$ is the fraction ϵ of the pile-up parameter μ visible to the detector and $\sigma_{\text{vis}} = \epsilon\sigma_{\text{inel}}$ the visible inelastic cross section. If σ_{vis} is known, the currently recorded luminosity can be determined by measuring μ_{vis} . At the ATLAS experiment, the observed number of inelastic interactions per bunch crossing μ_{vis} is measured using dedicated detectors, as for example LUCID-2 [102], a forward Cherenkov-detector using the quartz windows from photomultipliers as Cherenkov medium. In order to use μ_{vis} as luminosity monitor, the respective detectors need to be calibrated through a measurement of the visible inelastic cross section σ_{vis} . This can be done using so-called van der Meer (vdM) scans [103, 104], in which the transverse distribution of protons in the bunches is inferred by measuring the relative interaction rates as a function of the transverse beam separation[†]. The algorithms used to determine the σ_{vis} calibration are described in Refs. [100, 101]. The luminosity during the vdM runs can then be determined using eq. (2.1). At the LHC, vdM scans are typically performed in special low- μ runs with well-known machine parameters in order to minimise uncertainties [100]. During high- μ physics runs, a luminosity measurement is obtained through an extrapolation from the vdM runs.

The LHC entered operation in 2008, with first beams in September and first collisions by the end of November that same year [105]. Its operation is in general structured into so-called *Runs*, that are spanned by multiple years of data-taking. Run 1 spanned from 2009 to 2013 and delivered roughly 28.5 fb^{-1} of pp collision data to ATLAS, taken at centre-of-mass energies of 7 TeV and 8 TeV [106, 107, 101]. Run 2 lasted from 2015 to 2018 and saw a centre-of-mass energy increase to 13 TeV, delivering approximately 156 fb^{-1} of pp collision data to ATLAS [100]. Run 3 of pp collision data taking with two times design peak luminosity is currently planned to start its physics program in 2022 and last until the end of 2024 [108]. Current plans foresee Run 3 to deliver about 150 fb^{-1} of pp collision data with centre-of-mass energies of 13 TeV and 14 TeV. After Run 3, the LHC will be upgraded to the High Luminosity LHC (HL-LHC), significantly increasing the peak instantaneous luminosity and delivering up to 3000 fb^{-1} of pp collision data from 2027 until 2040 [108, 109].

This work uses pp collision data taken by ATLAS during Run 2 of the LHC. Of the 156 fb^{-1} delivered to ATLAS, 147 fb^{-1} were recorded, and 139 fb^{-1} were deemed to be good for physics analysis. Figure 2.3 shows the cumulative luminosity delivered to ATLAS during Run 2. Uncertainties on the measured total recorded luminosity stem from the measurements of μ_{vis} and σ_{vis} , but are dominated by the uncertainties on σ_{vis} as vdM scans can only be done during special runs with more or less fixed machine parameters, while the general conditions during high- μ conditions change continuously. For the full Run 2 dataset, the uncertainties accumulate to $\pm 1.7\%$ [100].

[†] This procedure is often referred to as *beam sweeping*.

2.2 ATLAS Experiment

The ATLAS experiment is one of two general-purpose detectors at the LHC. Located at Point 1 in a cavern 100 m below the surface, it is approximately 44 m long and 25 m high [90]. The design of the ATLAS experiment is driven by the aim to allow for a diverse research program, including SM precision measurements, Higgs physics and searches for BSM physics, whilst at the same time taking into account the unique and challenging conditions set by the LHC. The various detector technologies used are designed to withstand the high-radiation environment of the LHC, while allowing particle measurements with high spatial and temporal granularity. The general structure of ATLAS is depicted in fig. 2.4, and consists of a central part, called *barrel*, that has a cylindrical shape around the beam pipe, and two discs, called *end-caps*, that close off the barrel on each side. This makes the ATLAS detector forward-backward symmetric with a coverage of nearly full solid angle of 4π , which is needed in order to measure momentum imbalances caused by particles that only interact weakly with the detector material.

The interface between the ATLAS experiment and the LHC is the beam pipe. In order to be maximally transparent to the particles created in the collisions, but also be able to withstand the forces from the vacuum, the beam pipe is made out of Beryllium close to the interaction point (IP), and stainless-steel further away from the IP [1].

The following sections introduce the working principles of the different detector components used in ATLAS, starting with the innermost component closest to the IP, the inner detector, followed by the calorimeters in the middle and finally the muon spectrometers on the outside. If not otherwise stated, details on the detector components including the design parameter values are extracted from Ref. [90].

2.2.1 Coordinate system

In order to properly describe collision events in the ATLAS detector, a suitable detector system is needed. The right-handed coordinate system [111] used in ATLAS has its origin at the nominal IP in the centre of the detector. The positive x -axis points towards the centre of the LHC ring, the positive y -axis points upwards to the surface, and the beam pipe is used to define the z -axis. In the x - y plane, called the transverse plane, the azimuthal angle ϕ is the angle around the beam axis, and the polar angle θ is measured from the beam axis. The rapidity v [7] is defined as

$$v = \frac{1}{2} \ln \left(\frac{E + p_z}{E - p_z} \right) = \tanh^{-1} \frac{p_z}{E}, \quad (2.4)$$

with E the energy of an object and p_z its momentum in z -direction. As opposed to the polar angle θ , differences in the rapidity are invariant under Lorentz boosts in z -direction.

The pseudorapidity η [7] is the high-energy limit ($p \gg m$) of the rapidity, and defined as

$$\eta = -\ln \tan \frac{\theta}{2}, \quad (2.5)$$

with $\cos \theta = p_z/p$. Pseudorapidity and rapidity are approximately equal in the limit where $p \gg m$ and $\theta \gg \frac{1}{\gamma}$. Compared to the rapidity, the pseudorapidity has the advantage of not depending on the energy and momentum calibration of the detected objects. Additionally, it

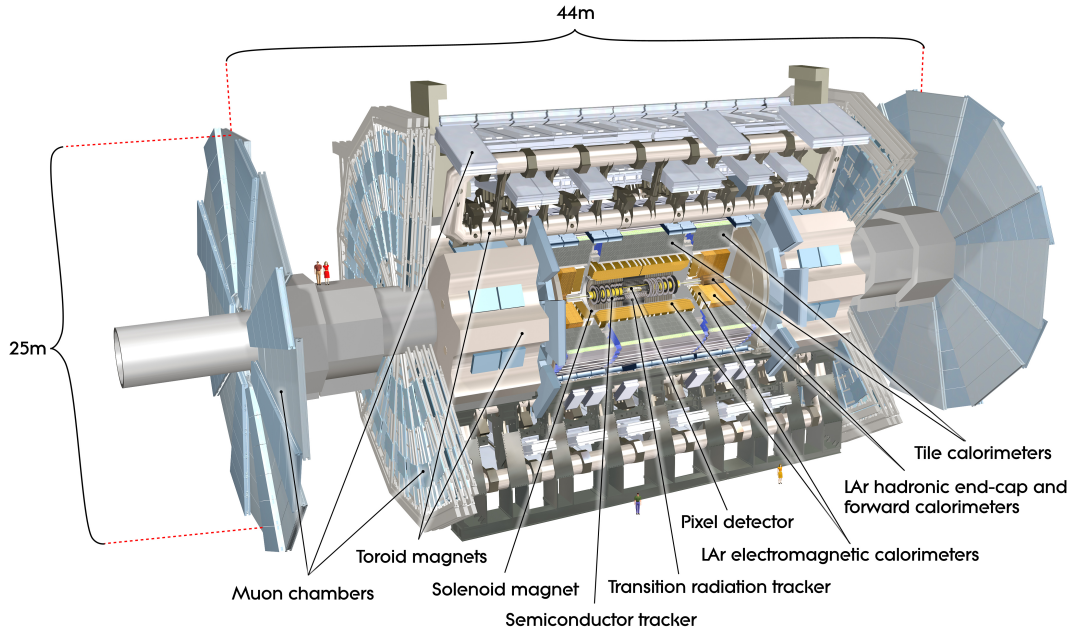


Figure 2.4: Computer generated picture of the ATLAS detector, giving an overview of the various subsystems [110].

gives a direct correspondence to the polar angle θ through the relation $\tanh \eta = \cos \theta$. Objects travelling along the beam axis have a pseudorapidity of $\eta = \infty$ and objects travelling in the x - y plane have $\eta = 0$.

The distance ΔR between two objects in the detector is given by

$$\Delta R = \sqrt{(\Delta\eta)^2 + (\Delta\phi)^2}. \quad (2.6)$$

The longitudinal momentum of the partons composing the colliding hadrons is only known by means of the Parton Distribution Functions (PDFs), giving the probabilities of the partons to have a certain energy in the direction of the beam. Thus, the total longitudinal energy in each collision is not exactly known, impeding the use of physics quantities in the z -direction. In the x - y plane, however, momentum conservation can be applied, which is why mainly transverse physics quantities are used, indicated by a subscript ‘T’, e.g. E_T or p_T .

2.2.2 Magnet system

In order to perform precise momentum measurements of particles, ATLAS uses a system of magnets, whose magnetic fields force charged particles on curved tracks due to the Lorentz force. Using precise measurements of the tracks taken in the inner detector and the muon spectrometers, the curvature of the tracks can be determined, allowing an inference of the charge-to-momentum ratio q/p of charged particles. ATLAS employs a set of four superconducting magnets, one central solenoid, and three toroids, all operating at a nominal temperature of 4.5 K, achieved through a cryogenic system using liquid helium.

The solenoid is aligned on the beam axis and provides a 2 T magnetic field for the inner detector. As it is located in front of the calorimeters (as seen from the IP), it is specially designed to have minimal material thickness in order to avoid influencing the subsequent energy measurements. The solenoid consists of single-layer coils made of a Nb/Ti conductor and additional aluminium for stability. It operates at a nominal current of 7.73 kA and uses the hadronic calorimeter as return yoke.

The toroid magnets consist of a barrel toroid and two end-cap toroids, producing a magnetic field of 0.5 T and 1 T for the muon spectrometers in the barrel and end-caps, respectively[†]. Both barrel and end-cap toroids consist of Nb/Ti/Cu conductors with aluminium stabilisation, wound into double pancake-shaped coils. The barrel toroid coils are enclosed in eight stainless-steel vacuum vessels in a racetrack-shaped configuration and arranged around the barrel calorimeters with an azimuthal symmetry. Aluminium-alloy struts provide the support structure necessary for the vessels to withstand the inward-directed Lorentz force of 1400 t in addition to their own weight. For the same reasons, the end-cap toroid coils are assembled in eight square units, and bolted and glued together with eight wedges, forming rigid structures. Both end-cap and barrel toroids operate at a nominal current of 20.5 kA.

2.2.3 Inner detector

Embedded in the magnetic field of the solenoid, the inner detector (ID) measures tracks of charged particles, allowing a determination of their momentum, while also providing crucial information for vertex reconstruction. As the ID is the detector closest to the beam pipe, its components need to be able to withstand the extreme high-radiation environment close to the IP. The ID consists of three subdetectors and uses two different working principles: semiconductor and gaseous detectors. In semiconductor-based tracking detectors, charged particles passing through the detector create a trail of electron-hole pairs that subsequently drift through the semiconductor material and cause electric signals. In gaseous detectors, traversing particles create electron-ion pairs that drift towards metal electrodes and induce electric signals.

Closest to the ID lies the pixel detector, followed by the silicon microstrip tracker (SCT), both of which are made of semiconductors. The SCT is surrounded by the transition radiation tracker (TRT), a gaseous detector. In total, the ID provides tracking and momentum information up to $|\eta| < 2.5$ and down to transverse momenta of nominally 0.5 GeV. A schematic illustration of the ID and its subdetectors is shown in fig. 2.5.

Pixel detector

In the high-rate environment directly adjacent to the beam pipe, the only detector technology able to operate and deliver high-precision tracking information over extended periods of time are semiconductor detectors segmented into pixels. As opposed to strip detectors, the reduced size of silicon pixel detectors and thus the significantly reduced hit rate per readout channel allows pixel detectors to be operational in the harsh environment close to the IP. In ATLAS, pixels are hybrids of silicon sensors and readout electronics bonded together, and were originally

[†] The magnetic field in of the toroid magnets is designed to be higher in the end-caps in order to ensure sufficient bending power for precise momentum measurements.

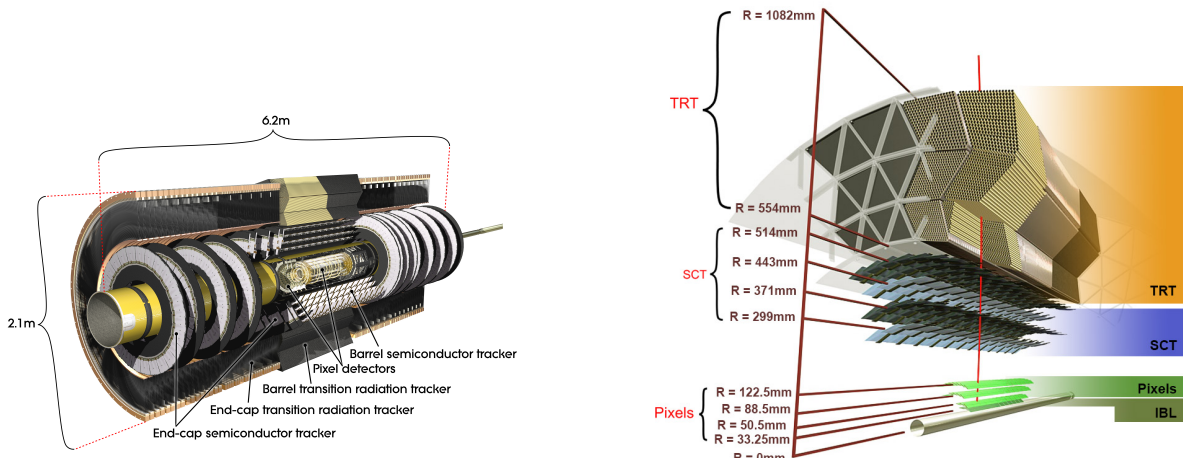


Figure 2.5: Schematic drawing of the ID and its subdetectors. Images adapted from [112, 113].

arranged in three layers in the barrel and the end-caps with a typical pixel of $50\text{ }\mu\text{m} \times 400\text{ }\mu\text{m}$, covering pseudorapidities up to $|\eta| < 2.5$. In order to increase robustness and performance in the high-luminosity environment, a new innermost layer, called the insertable B-layer (IBL), was installed together with a new, smaller radius beam pipe between Run 1 and Run 2 [114, 115]. The IBL uses smaller pixels with a size of $50\text{ }\mu\text{m} \times 250\text{ }\mu\text{m}$ and improves the tracking precision as well as vertex identification performance [115]. It also improves the performance of identifying jets originating from b -quarks (through a procedure called b -tagging, see ??) [116]. The tracking precision obtained by the pixel detector is $10\text{ }\mu\text{m}$ in $R-\phi$ and $115\text{ }\mu\text{m}$ in z for the barrel and R for the end-caps.

Silicon microstrip detector

The pixel detector is surrounded by the SCT, consisting of four layers in the barrel and nine disks in each of the end-caps. In order to provide two-dimensional tracking information, strips are arranged in double-layers with a small crossing angle of 40 mrad and a mean pitch of $80\text{ }\mu\text{m}$. A charged particle traversing the SCT through the barrel thus creates four space point measurements. In the barrel, one set of strips in each of the four double-layers is oriented in beam direction, thereby measuring the $R-\phi$ plane, and in the end-caps, one set of strips in each layer is oriented in radial direction. The SCT has roughly 6.3 million readout channels and provides tracking information up to $|\eta| < 2.5$. It achieves a precision of $17\text{ }\mu\text{m}$ in $R-\phi$ and $580\text{ }\mu\text{m}$ in z for the barrel and R for the end-caps.

Transition radiation tracker

The last and also largest of the three subdetectors of the ID is the TRT, a gaseous detector made of multiple layers of 4 mm diameter drift tubes, surrounding the pixel detector and the SCT. The drift tubes consist of an aluminium cathode coated on a polyimide layer reinforced by carbon fibres and use a gold-plated tungsten wire as anode. The tubes are filled with a Xe-based gas mixture, providing an electric permittivity different from the surrounding material, causing transition radiation when traversed by ultra-relativistic particles. While the 73 layers

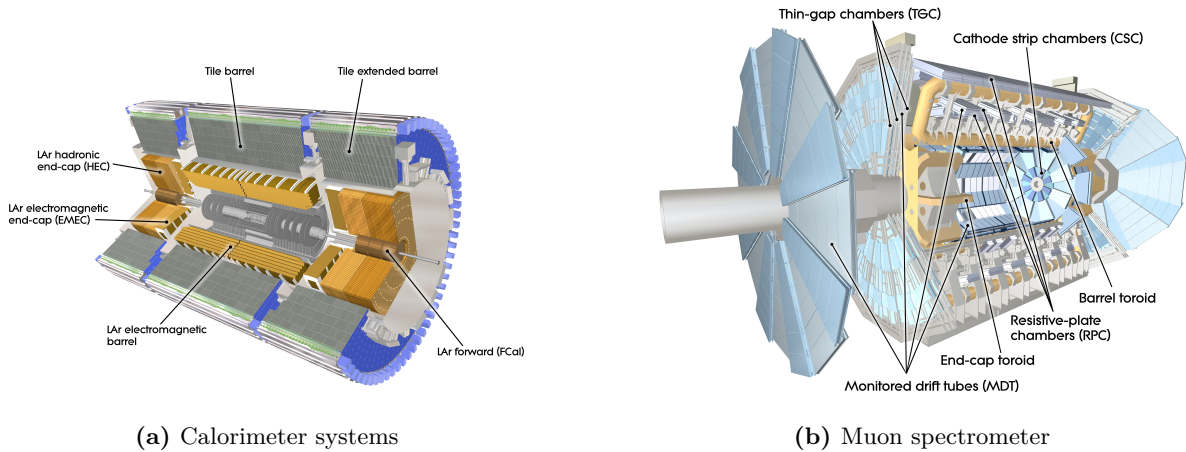


Figure 2.6: Schematic drawing of the (a) calorimeter systems and (b) the muon spectrometer in ATLAS. Images adapted from Refs. [118, 119].

of 144 cm long tubes in the barrel region are aligned parallel to the beam pipe, the 160 layers of 37 cm long tubes in the end-caps are aligned in radial direction, providing coverage up to $|\eta| < 2.0$ and an intrinsic accuracy of 130 μm in $R - \phi$. The low accuracy compared to the pixel detector and the SCT is compensated by the large amount of hits (typically 36 per track) and the longer measured track length. As the amount of transition radiation given off by a particle, is proportional to its Lorentz factor γ [7], the TRT is also used to improve electron identification [117]. For the same momentum, electrons will have a higher Lorentz factor than the heavier, charged pions, and consequently give off more transition radiation.

2.2.4 Calorimeters

The primary goal of calorimeters is to measure the energies of incoming particles by completely absorbing them. As the energies of neutral particles cannot be measured by other means, calorimeters are especially important for jet energy measurements (which contain neutral hadrons) [1]. Since particles like photons and electrons interact mostly electromagnetically, while hadrons predominantly interact through the strong interaction, two different calorimeter types are adopted in ATLAS. For values in η matching the coverage of the ID, the electromagnetic calorimeter uses a finer granularity designed for precision measurements of electrons and photons. The subsequent hadronic calorimeter has a coarser granularity sufficient for the requirements of jet reconstruction and missing transverse momentum measurements. With a coverage up to $|\eta| < 4.9$, the calorimeter system in ATLAS provides the near hermetic energy measurements needed for the inference of missing transverse momentum created by neutrinos and other weakly interacting neutral particles.

Both calorimeters are sampling calorimeters, consisting of alternating layers of active and absorbing material. The absorbing material interacts with the incoming particles, causing them to deposit their energy by creating cascades (often called *showers*) of secondary particles. The active layers are then used to record the shape and intensity of the showers produced. This alternating structure results in reduced material costs but also reduced energy resolution as only part of the particle's energy is sampled. Due to the typically longer cascades in

hadronic interactions compared to electromagnetic ones, and in order to minimise punch-through into the muon system, the hadronic calorimeter requires a greater material depth than the electromagnetic one. The calorimeter systems in ATLAS are schematically illustrated in fig. 2.6(a).

Electromagnetic calorimeter

The Electromagnetic (EM) calorimeter uses liquid argon (LAr) as active material and lead as absorber. Due to its accordion-shaped geometry, it provides full ϕ symmetry without azimuthal cracks. It is divided into a barrel part and two end-caps, covering $|\eta| < 1.475$ and $1.375 < |\eta| < 3.2$, respectively, and arranged in a way to provide uniform performance and resolution as a function of ϕ . The barrel EM calorimeter consists of two identical half-barrels with a small gap of 4 cm at $z = 0$. In the end-caps, the electromagnetic end-cap calorimeter (EMEC) consists of two coaxial wheels, covering the region $1.375 < |\eta| < 2.5$ and $2.5 < |\eta| < 3.2$, respectively. Calorimeter cells in the EM calorimeter are segmented into multiple layers with fine granularity in first layers in the η region matching the ID, and coarser granularity in the outer layers and for $2.5 < |\eta| < 3.2$. In order to offer good containment of electromagnetic showers, the EM calorimeter has a depth of at least 22 (24) radiation lengths in the barrel (end-caps). A single instrumented LAr layer serves as presampler in the region with $|\eta| < 1.8$, allowing measurements of the energy losses upstream of the EM calorimeter, as for example in the cryostats. The design energy resolution of the EM calorimeter is $\sigma_E/E = 10\%/\sqrt{E} \oplus 0.7\%$.

Hadronic calorimeter

Placed directly outside the envelope of the EM calorimeter is the hadronic tile calorimeter. It uses steel plates as absorber and polystyrene-based scintillating tiles as active material, and is subdivided into one central and two extended barrels. Each barrel is segmented in three layers in depth with a total thickness of 7.4 interaction lengths. The tiles are oriented radially and perpendicular to the beam pipe and grouped in 64 tile modules per barrel, resulting in a near hermetic azimuthal coverage. Wavelength shifting fibres are used to shift the ultraviolet light produced in the scintillator to visible light and guide it into photomultipliers located at the radially far end of each module. The tile calorimeter covers a region with $|\eta| < 1.7$ and has a granularity of $\Delta\eta \times \Delta\phi = 0.1 \times 0.1$ except for the outermost layer which has a slightly coarser granularity in η . The design energy resolution of the tile calorimeter is $\sigma_E/E = 56.4\%/\sqrt{E} \oplus 5.5\%$.

Hadronic calorimetry in the end-caps is provided by two independent calorimeter wheels per end-cap, situated directly behind the EMEC. Similar to the EMEC, the hadronic end-cap calorimeter (HEC) also uses LAr as active material, allowing both calorimeter systems to share a single cryostat per end-cap. Instead of lead, the HEC however uses copper as absorber, which not only drastically reduces the mass of a calorimeter at a given interaction length, but also improves the linearity of low-energy hadronic signals [120]. Each of the four wheels of the HEC is comprised of 32 wedge-shaped modules, divided into two layers in depth. The HEC provides coverage in the region with $1.5 < |\eta| < 3.2$, slightly overlapping with the tile calorimeter and thus reducing the drop in material density in the transition region. While the granularity in the precision region with $1.5 < |\eta| < 2.5$ is the same as for the tile calorimeter, more forward

regions with large $|\eta|$ have a granularity of $\Delta\eta \times \Delta\phi = 0.2 \times 0.2$. The design resolution of the HEC is $\sigma_E/E = 70.6\%/\sqrt{E} \oplus 5.8\%$.

Forward Calorimeter

The forward region with $3.1 < |\eta| < 4.9$ is covered by the LAr forward calorimeter (FCal), which is integrated into the end-cap cryostats. This hermetic design not only minimises energy losses in cracks between the calorimeter systems, but also reduces the amount of background reaching the muon system in the outer shell of the ATLAS experiment. In order to limit the amount of neutrons reflected into the ID, the FCal is recessed by about 1.2 m with respect to the EM calorimeter, motivating a high-density design due to space constraints. The FCal in each end-cap consists of three layers with a total depth of 10 interaction lengths. While the first layer uses copper as absorber and is optimised for electromagnetic measurements, the remaining two layers are made of tungsten and cover hadronic interactions. The metals comprising each layer are arranged in a matrix structure with electrodes consisting of rods and tubes parallel to the beam pipe filling out regular channels. The small gaps (0.25 mm in the first layer) between the rods and tubes of the electrodes are filled with LAr as active material.

2.2.5 Muon spectrometer

Muons, being minimum ionising particles, are the only charged particles that consistently pass through the entire detector including the calorimeter system. Providing one of the cleanest signatures for BSM physics [1], muonic final states are measured with a dedicated detector system on the outermost layer of the ATLAS experiment. Embedded in the magnetic field of the toroid magnets, the muon spectrometer (MS) consists of three concentric cylindrical layers in the barrel region, and three wheels in each end-cap, providing momentum measurements up to $|\eta| < 2.7$. It is designed to deliver a transverse momentum resolution of 10% for 1 TeV tracks and be able to measure muon momenta down to roughly 3 GeV.

The MS uses two high-precision gaseous detector chamber types, Monitored Drift Tube (MDT) chambers and Cathode Strip Chambers (CSCs). As both the MDTs and CSCs are drift chambers relying on charges drifting to an anode or cathode, the maximum response times of 700 ns and 50 ns, respectively, are slow compared to the bunch-spacing of 25 ns. ATLAS therefore uses Resistive Plate Chambers (RPCs) in the barrel and Thin Gap Chambers (TGCs) in the end-caps as triggers in order to associate measurements to the right bunch-crossing.

Monitored drift tubes

The MDT chambers are the main subcomponent providing precision measurements of the muon tracks up to $|\eta| < 2.7$, except in the innermost end-cap layer where their coverage only extends to $|\eta| < 2.0$. The MDT are made of 3–4 layers of ~ 30 mm diameter drift tubes operated with Ar/CO₂ gas[†] pressurised to 3 bar. Charged particles traversing the drift tubes ionise the gas, creating electrons that drift towards a central tungsten-rhenium anode wire with a diameter of 50 µm. Following the symmetry of the barrel toroid magnet, the MDT chambers are arranged

[†] With a small admixture of 300 ppm of water to improve high voltage stability.

as octets around the calorimeters with the drift tubes in ϕ direction, i.e. tangential to circles around the beam pipe. In order to be able to correct for potential chamber deformations due to varying thermal gradients, each MDT chamber is equipped with an internal optical alignment system. Apart from the regular chambers in the barrel and the end-cap wheels, special modules are installed in order to minimise the acceptance losses due to the ATLAS support structure (the *feet* of the experiment). With a single-tube accuracy of 80 μm , two combined 3 (4)-tube multi-layers yield a resolution of 35 (30) μm . As MDT chambers only provide precision measurement in η , information in ϕ is taken from the RPCs and TGCs.

Cathode strip chambers

In the region with $|\eta| > 2.0$ in the first layer of the end-caps, the particle flux is too high to allow for safe operation of MDT chambers. Instead, CSCs, multiwire proportional chambers, are used for precision measurements in this region. The gold-plated tungsten-rhenium anode wires in the CSCs have a diameter of 30 μm and are oriented in radial direction. The wires are enclosed on both sides by cathode planes, one segmented perpendicular to the wires (thus providing the precision coordinate), the other parallel to the wires. Each chamber is filled with an Ar/CO₂ gas mixture and consists of four wire planes, resulting in four measurements of η and ϕ for each track. In addition to the chamber-internal alignment sensors, ATLAS also employs an optical alignment system in order to align the precision chambers to each other. The CSCs provide a resolution of about 45 μm in R and 5 mm in ϕ .

Resistive plate chambers

RPCs are gaseous parallel electrode-plate chambers filled with a non-flammable low cost tetrafluorethane-based gas mixture. They use two resistive plastic laminate plates kept 2 mm apart by insulating spacers. Due to an electric field of roughly 4.9 kV mm⁻¹ between the plates, charged particles traversing the chamber cause avalanches of charges that can be read out through capacitive coupling to metallic strips mounted on the outside of the resistive plates. In order to provide tracking information in both coordinates, each RPC consists of two rectangular units each containing two gas volumes with a total of four pairwise orthogonal sets of readout strips. The three concentric cylindrical layers of RPCs in the barrel region cover $|\eta| < 1.05$ and provide six measurements of η and ϕ .

Thin gap chambers

The TGCs are not only necessary for triggering in the end-cap MS but also provide measurements of a second coordinate orthogonal to the measurements of the MDTs. TGCs are multi-wire proportional chambers enclosed by two cathode planes and a wire-to-wire gap of 1.8 mm. The gas mixture of CO₂ and n-pentane allows for a quasi-saturated operation mode resulting in a relatively low gas gain. Each TGC unit is built from a doublet or triplet of such chambers, separated by a supporting honeycomb structure. In each unit, the azimuthal coordinate is measured by radial copper readout strips, while the bending coordinate is provided by the wire groups. The TGCs are mounted in two concentric disks in each end-cap, one covering the rapidity range $1.05 < |\eta| < 1.92$ and one covering the more forward region $1.92 < |\eta| < 2.4$.

2.2.6 Forward detectors

Apart from the relative luminosity monitor LUCID-2 [102] (introduced in section 2.1.2) located at ± 17 m from the IP, ATLAS uses three additional small detectors in the forward region. At ± 140 m from the IP, immediately behind the location where the straight beam pipe splits back into two separate beam pipes, lies the Zero-Degree Calorimeter (ZDC) [121]. The ZDC is embedded in a neutral particle absorber and mainly measures forward neutrons with $|\eta| > 8.3$ in heavy-ion collisions. Even further out from the IP at ± 240 m, lies the Absolute Luminosity for ATLAS (ALFA) detector [122], consisting of scintillating fibre trackers placed in Roman pots [123] measuring the absolute luminosity through small scattering angles of $3 \mu\text{rad}$ (necessitating the special beam conditions also used for the LUCID-2 calibrations). The last of the forward detectors is the ATLAS Forward Proton (AFP) [124] detector, installed at the end of 2016 and operational since early 2017, situated ± 205 m and ± 217 m from the IP. It consists of Roman pots containing silicon trackers and time-of-flight detectors and allows to study very forward protons from elastic and diffractive scattering processes.

2.2.7 Trigger and data acquisition system

With a nominal bunch spacing of 25 ns, the bunch crossing rate within ATLAS is 40 MHz. Even with only a single pp collision event per bunch crossing, a mean event size of ~ 1.6 MB would result in a data volume of more than 60 TB per second. Building and maintaining computing and storage facilities able to handle this bandwidth would significantly exceed the available resources. Luckily, interesting[†] physics events will often only occur at relatively low rates, and generally be hidden in vast amounts of QCD processes that have much higher cross-sections. In order to reduce the event rate written to disk and focus on interesting signatures worth studying, ATLAS used a two-level *trigger* system during the Run 2 data-taking period [125]. The general approach is to buffer events into temporary memory until the trigger system has decided to keep or discard them. The size of the temporary memory directly dictates the latency available to the trigger system for making a decision.

The Level 1 (L1) trigger [126] is the first stage of the trigger system. It is hardware-based and uses only coarse granularity calorimeter and muon detector information. With the inclusion of the Level-1 Topological Processor (L1Topo) [127] in Run 2, the L1 trigger is able to exploit topological features based on angular and kinematic selections and defines Regions of Interest (ROIs), i.e. regions in η and ϕ with interesting properties, that will be further analysed by the subsequent trigger step. Memory constraints allow for a decision time of 2.5 μs per event, thus the L1 trigger reduces the event rate from the bunch-crossing rate of 40 MHz to 100 kHz.

The ROIs generated by the L1 trigger are subsequently processed by the High Level Trigger (HLT) [128], a software-based trigger running on a dedicated computing farm. The HLT has access to the full detector granularity in the ROIs as well as the entire event and runs reconstruction algorithms similar to those used in offline analysis, allowing to significantly refine the decisions from the L1 trigger. The HLT reduces the event rate from 100 kHz to 1 kHz. Events that pass one of the HLT chains are written to permanent storage at CERN. Data flow from the detectors to the storage elements and between the L1 and HLT trigger elements is handled by the Data Acquisition System (DAQ) [128].

[†] Defining what is deemed to be interesting is to some extent up to the physics analysis groups

2.2.8 Monte Carlo simulation

Monte Carlo (MC) methods play a crucial role for simulating physics events in ATLAS. MC simulations are computational algorithms using repeated random sampling to solve complex problems, often the estimation of multi-dimensional integrals for which analytical solutions are not known. According to the law of large numbers, the numerical approximations obtained by such a stochastic method become more accurate, the larger the sample size is. In addition, the central limit theorem also allows to state an uncertainty on the estimation of an expected value. This method can in principle be used for any problem with a probabilistic interpretation and is therefore well suited for particle physics where many aspects are inherently connected to Probability Density Functions (pdfs).

In the ATLAS experiment, MC methods are not only used in physics analysis to estimate contributions from various physics processes in different phase space regions, but also to simulate particle interactions with the detector material. This method even finds ample applications in detector design and optimisation as well as physics objects reconstruction techniques. All of these applications rely on the MC simulations being as precise as possible, i.e. correctly describing the physics processes and detector responses underlying the data recorded by the ATLAS experiment. For reasons of efficient computing resource utilisation and easier software validation, the ATLAS simulation infrastructure [129] can be divided into three main steps:

- (i) Event generation,
- (ii) Detector simulation,
- (iii) Digitisation,

producing an output format identical to that of the DAQ for recorded pp collision events, such that the same trigger and reconstruction algorithms can be run on simulated data.

Event generation

Only a fraction of all pp events actually involve a *hard-scattering* event with high-momentum transfer, rendering them interesting for particle physicists to study. Generating and understanding the final states of these pp collision events is an enormously challenging problem as it typically involves hundreds of particles with energies spanning many orders of magnitude [131]. This makes the matrix elements connected to these processes too complicated to be computed beyond the first few orders of perturbation theory. The treatment of divergences and the integration over large phase spaces further complicates the calculation of experimental observables.

Due to the high-momentum transfer scale, the cross section of the hard-scatter interaction can be calculated perturbatively using collinear factorisation [131],

$$\sigma = \sum_{a,b} \int_0^1 dx_a dx_b \int d\Phi_n f_a^{h_1}(x_a, \mu_F) f_b^{h_2}(x_b, \mu_F) \times \frac{1}{2x_a x_b s} |\mathcal{M}_{ab \rightarrow n}|^2(\Phi_n; \mu_F, \mu_R), \quad (2.7)$$

where x_a and x_b the momentum fractions of the partons a and b with respect to their parent hadrons h_1 and h_2 , μ_F and μ_R are the unphysical factorisation and the renormalisation scales,

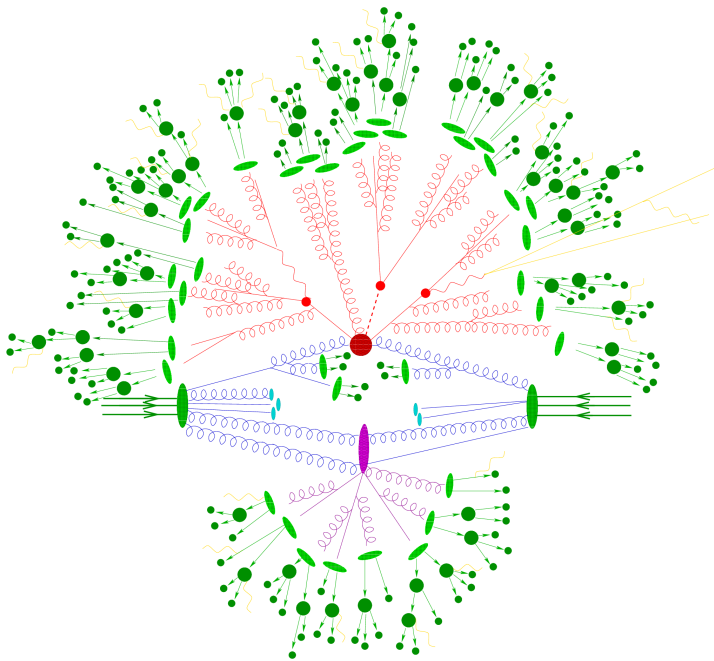


Figure 2.7: Pictorial representation of a $t\bar{t} + H$ event simulated by a MC event generator. The hard interaction (big red blob) is followed by the decay of the two top quarks and the Higgs boson (small red blobs). ISR and FSR are shown as curly blue and red lines, respectively. A second interaction is simulated (purple blob) and contributions from the underlying event are modelled (purple lines). The hadronisation of final-state partons (light green blobs) is followed by the decays of unstable hadrons (dark green blobs). QED radiation (yellow lines) is added at each stage of the event simulation. Figure adapted from [130].

respectively, and $d\Phi_n$ is the differential final state phase space element. The phase space integration is typically done using MC sampling methods. The choices for μ_R and μ_F are to some extent arbitrary, but are typically chosen to be in accordance with the logarithmic structure of quantum chromodynamics (QCD), such that the matrix elements can be combined with the subsequent parton showers [131]. The Matrix Element (ME) $|\mathcal{M}_{ab \rightarrow n}|^2$ can be calculated using different methods [131], with most MC generators employing leading order (LO) computations. As LO matrix elements are only reliable for the shapes of the distributions, an additional *K-factor* correcting the normalisation of the cross section to next-to-leading order (NLO) is typically used [131]. The probability of finding a parton with momentum fractions x in a hadron h , is given by the PDF $f_a^h(x, \mu_F)$ and depends on the probed factorisation scale μ_F . The PDFs depend on non-perturbative aspects of the proton wave function and can thus not be calculated from first principles. Instead, they are extracted from measurements in deep inelastic scattering experiments (see e.g. [132, 133]). The variety of PDFs provided by different groups, is accessible in a common format through a unified interface implemented by the LHAPDF library [134]. In MC generators, the choice of PDFs not only play a crucial role for the simulation of the hard process, but also in the subsequent parton showers and multiple parton interactions, thus influencing both cross sections and event shapes.

Fixed-order matrix elements work well for describing separated, hard partons but are not sufficient to describe soft and collinear partons. Higher order effects from gluon radiation can be simulated using a Parton Shower (PS) algorithm. The emitted gluons will radiate additional gluons or split into quark–antiquark pairs which can in turn undergo additional gluon radiation. The PS thus describes an evolutionary process in momentum transfer scales from the scale of the hard scatter interaction down to the infrared scale $\mathcal{O}(1\text{ GeV})$ where QCD becomes non-perturbative and partons are confined into hadrons. Both ISR and FSR are simulated through the PS. As opposed to ME calculations, PSs offer poor modelling of few hard partons, but excel in the simulation of collinear and soft multi-parton states.

In order to avoid double counting, the hard partons described by the calculation of the ME and the soft collinear emissions of the PS have to be connected to each other. This is done either through *matching* or *merging*. ME matching approaches [135] integrate higher-order corrections to an inclusive process with the PS [131]. Merging techniques like the CKKW [136] or CKKW-L [137] methods define an unphysical merging scale which can be understood as a jet resolution scale such that higher order ME corrections are only calculated for jets above that scale (while jets below that scale are modelled with the PS). Additional activity in the event not directly associated to the hard process is simulated. The underlying event is typically defined to be all additional activity after ISR and FSR off the hard process has been taken into account [131]. Furthermore, *multiple interactions* can occur in a single pp collision. The modelling of multiple interactions involves multiple hard scatter processes per pp collision as well as multiple soft interactions in addition to the hard scatter process.

Once the PS reaches energies of $\mathcal{O}(1 \text{ GeV})$, entering the non-perturbative regime of QCD, the coloured objects need to be transformed into colourless states. This so-called *hadronisation* step cannot be calculated from first principles but has to be modelled, typically with either a *string* or a *cluster* model. The most advanced of the string models is the *Lund* model [138, 139]. It starts from linear confinement and considers a linear potential between a $q\bar{q}$ pair, that can be thought of as a uniform colour flux tube stretching between the q and \bar{q} , with a transverse dimension of the order of typical hadronic size (i.e. around 1 fm). As the $q\bar{q}$ pair moves apart, the flux tube stretches in length, leading to an increase in potential energy, finally breaking apart once enough energy is available to create a new $q'\bar{q}'$ pair, resulting in two colourless quark pairs $q\bar{q}'$ and $q'\bar{q}$. The new quark pairs can again move apart and break up further, leading to quark anti-quark pairs with low relative momentum, forming the final hadrons. The cluster model is based on the preconfinement property of PSs [140], stating that the colourless clusters of partons can be formed at any evolution scale Q_0 of the PS, and result in universal invariant mass distributions that depend only on Q_0 and the QCD scale Λ , but not on the energy scale Q or nature of the hard process at the origin of the PS [131]. The universal invariant mass distribution holds in the asymptotic limit where $Q_0 \ll Q$. If further $Q_0 \gg \Lambda$, then the mass, momentum and multiplicity distributions of the colourless clusters can even be calculated perturbatively [131]. Cluster models start with non-perturbative splitting of gluons and $q\bar{q}$ pairs, followed by the formation of clusters from colour-connected pairs. Clusters further split up until the Q_0 scale is reached, at which point they form the final mesons.

As not all hadrons formed in the hadronisation process are stable, the affected hadrons need to be decayed until they form resonances stable enough to reach the detector material. In addition QED radiation, that can happen at any time during the event, needs to be simulated. This is typically either done with algorithms similar to the ones used for the PS, or using the Yennie–Frautschi–Suura formalism proposed in Ref. [141].

The simulation steps that cannot be performed from first principles but rely on phenomenological models (underlying event, PS, hadronisation) introduce free parameters that need to be derived or *tuned* from parameter optimisations against experimental data. In ATLAS, the output of MC event generators is stored in so-called EVNT data format containing HepMC-like [142] event records. Although only the stable final-state particles are propagated to the detector simulation, the original event record contains the entire connected tree as so-called *Monte Carlo truth*. A representation of a full simulated SUSY signal event considering the simplified model from fig. 1.8 is shown in fig. 2.8,

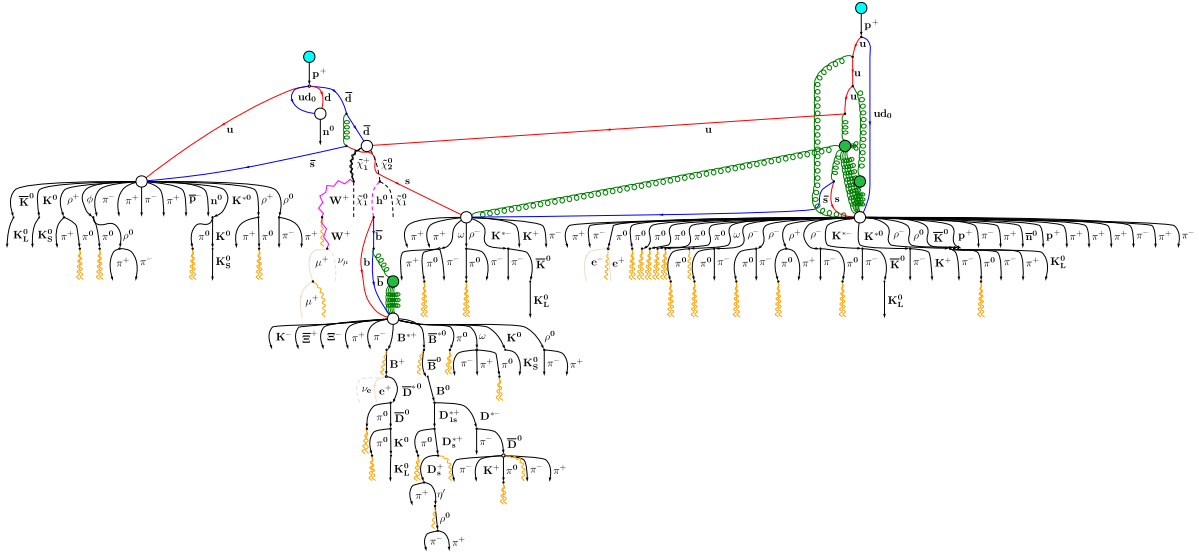


Figure 2.8: Pictorial representation of a (relatively simple) fully showered electroweakino pair production event with a final state including an electron and two b -jets. Most of the additional activity in the event stems from QCD interactions and results in a large amount of hadrons in the final state. The two incoming protons are marked as blue blobs. Gluons are represented as green curly green lines, and gluon self interaction is shown as green blobs (indicating only initial and final particles). Gauge and Higgs bosons are shown as pink lines. Photon radiation is shown as curly yellow lines.

Detector simulation

Only the final-state particles generated by the MC event generator are read into the detector simulation. In ATLAS, the full detector simulation is handled by GEANT4 [143], a toolkit providing detailed models for physics processes as well as an infrastructure for particle transportation through a given geometry. GEANT4 has knowledge about the full detector geometry as well as the materials used in the subdetectors and is able to compute the energy deposits (so-called *hits*) from single particles in the different sensitive portions of the detector components. The GEANT4 simulation adds information to the Monte Carlo truth content created during the event generation, including however only the most relevant tracks (mostly from the ID) due to size constraints [129].

The complicated detector geometry and the detailed description of physics processes requires large computing resources for the full detector simulation using GEANT4, rendering it inaccessible for many physics studies requiring large statistics. Several varieties of fast simulations are available as an alternative. One of the most-used ones is ATLFAST-II [129], a fast simulation that uses the GEANT4 full simulation only for the ID and MS. The slow simulation in the calorimeters—taking about 80% of the full simulation time—is replaced with FASTCALOSIM [144], using parameterised electromagnetic and hadronic showers. Compared to the $\mathcal{O}(10^3)$ s simulation time per event in the full simulation, the ATLFAST-II detector simulation only takes $\mathcal{O}(10^2)$ s [129].

Digitisation

During the digitisation step, the hits from the detector simulation are converted into detector responses, so-called *digits* that are typically produced when currents or voltages in the respective readout channels rise above a certain threshold in a given time window. The digitisation considers a modelling of the peculiarities of each detector component, including electronic noise and cross-talk [129]. The effects from out-of-time and in-time pile-up are also considered by reading in multiple events and overlaying their hits. In order to match the true pile-up distribution in data, the number of events to overlay per bunch crossing can be set at run time. As described in section 2.1.1, effects from cavern background, beam halo and beam gas can either be mitigated or removed at analysis level and are therefore typically not simulated.

Bibliography

- [1] I. C. Brock and T. Schorner-Sadenius, *Physics at the terascale*. Wiley, Weinheim, 2011. <https://cds.cern.ch/record/1354959>.
- [2] M. E. Peskin and D. V. Schroeder, *An Introduction to quantum field theory*. Addison-Wesley, Reading, USA, 1995. <http://www.slac.stanford.edu/~mpeskin/QFT.html>.
- [3] S. P. Martin, “A Supersymmetry primer,” [arXiv:hep-ph/9709356 \[hep-ph\]](https://arxiv.org/abs/hep-ph/9709356). [Adv. Ser. Direct. High Energy Phys.18,1(1998)].
- [4] M. Bustamante, L. Cieri, and J. Ellis, “Beyond the Standard Model for Montaneros,” in *5th CERN - Latin American School of High-Energy Physics*. 11, 2009. [arXiv:0911.4409 \[hep-ph\]](https://arxiv.org/abs/0911.4409).
- [5] L. Brown, *The Birth of particle physics*. Cambridge University Press, Cambridge Cambridgeshire New York, 1986.
- [6] P. J. Mohr, D. B. Newell, and B. N. Taylor, “CODATA Recommended Values of the Fundamental Physical Constants: 2014,” *Rev. Mod. Phys.* **88** no. 3, (2016) 035009, [arXiv:1507.07956 \[physics.atom-ph\]](https://arxiv.org/abs/1507.07956).
- [7] P. D. Group, “Review of Particle Physics,” *Progress of Theoretical and Experimental Physics* **2020** no. 8, (08, 2020), <https://academic.oup.com/ptep/article-pdf/2020/8/083C01/34673722/ptaa104.pdf>. <https://doi.org/10.1093/ptep/ptaa104>. 083C01.
- [8] **Super-Kamiokande** Collaboration, Y. Fukuda *et al.*, “Evidence for oscillation of atmospheric neutrinos,” *Phys. Rev. Lett.* **81** (1998) 1562–1567, [arXiv:hep-ex/9807003 \[hep-ex\]](https://arxiv.org/abs/hep-ex/9807003).
- [9] Z. Maki, M. Nakagawa, and S. Sakata, “Remarks on the unified model of elementary particles,” *Prog. Theor. Phys.* **28** (1962) 870–880. [,34(1962)].
- [10] N. Cabibbo, “Unitary symmetry and leptonic decays,” *Phys. Rev. Lett.* **10** (Jun, 1963) 531–533. <https://link.aps.org/doi/10.1103/PhysRevLett.10.531>.
- [11] M. Kobayashi and T. Maskawa, “CP Violation in the Renormalizable Theory of Weak Interaction,” *Prog. Theor. Phys.* **49** (1973) 652–657.
- [12] E. Noether and M. A. Tavel, “Invariant variation problems,” [arXiv:physics/0503066](https://arxiv.org/abs/physics/0503066).
- [13] J. C. Ward, “An identity in quantum electrodynamics,” *Phys. Rev.* **78** (Apr, 1950) 182–182. <https://link.aps.org/doi/10.1103/PhysRev.78.182>.

- [14] Y. Takahashi, “On the generalized ward identity,” *Il Nuovo Cimento (1955-1965)* **6** no. 2, (Aug, 1957) 371–375. <https://doi.org/10.1007/BF02832514>.
- [15] G. ’tHooft, “Renormalization of massless yang-mills fields,” *Nuclear Physics B* **33** no. 1, (1971) 173 – 199. <http://www.sciencedirect.com/science/article/pii/0550321371903956>.
- [16] J. Taylor, “Ward identities and charge renormalization of the yang-mills field,” *Nuclear Physics B* **33** no. 2, (1971) 436 – 444. <http://www.sciencedirect.com/science/article/pii/0550321371902975>.
- [17] A. A. Slavnov, “Ward identities in gauge theories,” *Theoretical and Mathematical Physics* **10** no. 2, (Feb, 1972) 99–104. <https://doi.org/10.1007/BF01090719>.
- [18] C. N. Yang and R. L. Mills, “Conservation of isotopic spin and isotopic gauge invariance,” *Phys. Rev.* **96** (Oct, 1954) 191–195. <https://link.aps.org/doi/10.1103/PhysRev.96.191>.
- [19] K. G. Wilson, “Confinement of quarks,” *Phys. Rev. D* **10** (Oct, 1974) 2445–2459. <https://link.aps.org/doi/10.1103/PhysRevD.10.2445>.
- [20] T. DeGrand and C. DeTar, *Lattice Methods for Quantum Chromodynamics*. World Scientific, Singapore, 2006. <https://cds.cern.ch/record/1055545>.
- [21] S. L. Glashow, “Partial-symmetries of weak interactions,” *Nuclear Physics* **22** no. 4, (1961) 579 – 588. <http://www.sciencedirect.com/science/article/pii/0029558261904692>.
- [22] S. Weinberg, “A model of leptons,” *Phys. Rev. Lett.* **19** (Nov, 1967) 1264–1266. <https://link.aps.org/doi/10.1103/PhysRevLett.19.1264>.
- [23] A. Salam and J. C. Ward, “Weak and electromagnetic interactions,” *Il Nuovo Cimento (1955-1965)* **11** no. 4, (Feb, 1959) 568–577. <https://doi.org/10.1007/BF02726525>.
- [24] C. S. Wu, E. Ambler, R. W. Hayward, D. D. Hoppes, and R. P. Hudson, “Experimental test of parity conservation in beta decay,” *Phys. Rev.* **105** (Feb, 1957) 1413–1415. <https://link.aps.org/doi/10.1103/PhysRev.105.1413>.
- [25] M. Gell-Mann, “The interpretation of the new particles as displaced charge multiplets,” *Il Nuovo Cimento (1955-1965)* **4** no. 2, (Apr, 1956) 848–866. <https://doi.org/10.1007/BF02748000>.
- [26] K. Nishijima, “Charge Independence Theory of V Particles*,” *Progress of Theoretical Physics* **13** no. 3, (03, 1955) 285–304, <https://academic.oup.com/ptp/article-pdf/13/3/285/5425869/13-3-285.pdf>. <https://doi.org/10.1143/PTP.13.285>.
- [27] T. Nakano and K. Nishijima, “Charge Independence for V-particles*,” *Progress of Theoretical Physics* **10** no. 5, (11, 1953) 581–582, <https://academic.oup.com/ptp/article-pdf/10/5/581/5364926/10-5-581.pdf>. <https://doi.org/10.1143/PTP.10.581>.
- [28] F. Englert and R. Brout, “Broken symmetry and the mass of gauge vector mesons,” *Phys. Rev. Lett.* **13** (Aug, 1964) 321–323. <https://link.aps.org/doi/10.1103/PhysRevLett.13.321>.
- [29] P. W. Higgs, “Broken symmetries and the masses of gauge bosons,” *Phys. Rev. Lett.* **13** (Oct, 1964) 508–509. <https://link.aps.org/doi/10.1103/PhysRevLett.13.508>.

- [30] P. W. Higgs, “Spontaneous symmetry breakdown without massless bosons,” *Phys. Rev.* **145** (May, 1966) 1156–1163. <https://link.aps.org/doi/10.1103/PhysRev.145.1156>.
- [31] Y. Nambu, “Quasiparticles and Gauge Invariance in the Theory of Superconductivity,” *Phys. Rev.* **117** (1960) 648–663. [[132\(1960\)](#)].
- [32] J. Goldstone, “Field Theories with Superconductor Solutions,” *Nuovo Cim.* **19** (1961) 154–164.
- [33] V. Brdar, A. J. Helmboldt, S. Iwamoto, and K. Schmitz, “Type-I Seesaw as the Common Origin of Neutrino Mass, Baryon Asymmetry, and the Electroweak Scale,” *Phys. Rev. D* **100** (2019) 075029, [arXiv:1905.12634 \[hep-ph\]](https://arxiv.org/abs/1905.12634).
- [34] G. ’t Hooft and M. Veltman, “Regularization and renormalization of gauge fields,” *Nuclear Physics B* **44** no. 1, (1972) 189 – 213. <http://www.sciencedirect.com/science/article/pii/0550321372902799>.
- [35] F. Zwicky, “Die Rotverschiebung von extragalaktischen Nebeln,” *Helv. Phys. Acta* **6** (1933) 110–127. <https://cds.cern.ch/record/437297>.
- [36] V. C. Rubin and W. K. Ford, Jr., “Rotation of the Andromeda Nebula from a Spectroscopic Survey of Emission Regions,” *Astrophys. J.* **159** (1970) 379–403.
- [37] G. Bertone, D. Hooper, and J. Silk, “Particle dark matter: Evidence, candidates and constraints,” *Phys. Rept.* **405** (2005) 279–390, [arXiv:hep-ph/0404175](https://arxiv.org/abs/hep-ph/0404175).
- [38] D. Clowe, M. Bradac, A. H. Gonzalez, M. Markevitch, S. W. Randall, C. Jones, and D. Zaritsky, “A direct empirical proof of the existence of dark matter,” *Astrophys. J.* **648** (2006) L109–L113, [arXiv:astro-ph/0608407 \[astro-ph\]](https://arxiv.org/abs/astro-ph/0608407).
- [39] A. Taylor, S. Dye, T. J. Broadhurst, N. Benitez, and E. van Kampen, “Gravitational lens magnification and the mass of abell 1689,” *Astrophys. J.* **501** (1998) 539, [arXiv:astro-ph/9801158](https://arxiv.org/abs/astro-ph/9801158).
- [40] C. Bennett *et al.*, “Four year COBE DMR cosmic microwave background observations: Maps and basic results,” *Astrophys. J. Lett.* **464** (1996) L1–L4, [arXiv:astro-ph/9601067](https://arxiv.org/abs/astro-ph/9601067).
- [41] G. F. Smoot *et al.*, “Structure in the COBE Differential Microwave Radiometer First-Year Maps,” *ApJS* **396** (September, 1992) L1.
- [42] **WMAP** Collaboration, “Nine-year Wilkinson Microwave Anisotropy Probe (WMAP) Observations: Final Maps and Results,” *ApJS* **208** no. 2, (October, 2013) 20, [arXiv:1212.5225 \[astro-ph.CO\]](https://arxiv.org/abs/1212.5225).
- [43] **WMAP** Collaboration, “Nine-year Wilkinson Microwave Anisotropy Probe (WMAP) Observations: Cosmological Parameter Results,” *ApJS* **208** no. 2, (October, 2013) 19, [arXiv:1212.5226 \[astro-ph.CO\]](https://arxiv.org/abs/1212.5226).
- [44] **Planck** Collaboration, “Planck 2018 results. I. Overview and the cosmological legacy of Planck,” *Astron. Astrophys.* **641** (2020) A1, [arXiv:1807.06205 \[astro-ph.CO\]](https://arxiv.org/abs/1807.06205).
- [45] A. Liddle, *An introduction to modern cosmology; 3rd ed.* Wiley, Chichester, Mar, 2015. <https://cds.cern.ch/record/1976476>.
- [46] **Planck** Collaboration, “Planck 2018 results. VI. Cosmological parameters,” *Astron. Astrophys.* **641** (2020) A6, [arXiv:1807.06209 \[astro-ph.CO\]](https://arxiv.org/abs/1807.06209).

- [47] H. Georgi and S. L. Glashow, “Unity of all elementary-particle forces,” *Phys. Rev. Lett.* **32** (Feb, 1974) 438–441. <https://link.aps.org/doi/10.1103/PhysRevLett.32.438>.
- [48] I. Aitchison, *Supersymmetry in Particle Physics. An Elementary Introduction*. Cambridge University Press, Cambridge, 2007.
- [49] **Muon g-2** Collaboration, G. Bennett *et al.*, “Final Report of the Muon E821 Anomalous Magnetic Moment Measurement at BNL,” *Phys. Rev. D* **73** (2006) 072003, [arXiv:hep-ex/0602035](https://arxiv.org/abs/hep-ex/0602035).
- [50] H. Baer and X. Tata, *Weak Scale Supersymmetry: From Superfields to Scattering Events*. Cambridge University Press, 2006.
- [51] A. Czarnecki and W. J. Marciano, “The Muon anomalous magnetic moment: A Harbinger for ‘new physics’,” *Phys. Rev. D* **64** (2001) 013014, [arXiv:hep-ph/0102122](https://arxiv.org/abs/hep-ph/0102122).
- [52] J. L. Feng and K. T. Matchev, “Supersymmetry and the anomalous magnetic moment of the muon,” *Phys. Rev. Lett.* **86** (2001) 3480–3483, [arXiv:hep-ph/0102146](https://arxiv.org/abs/hep-ph/0102146).
- [53] S. Coleman and J. Mandula, “All possible symmetries of the s matrix,” *Phys. Rev.* **159** (Jul, 1967) 1251–1256. <https://link.aps.org/doi/10.1103/PhysRev.159.1251>.
- [54] R. Haag, J. T. Lopuszanski, and M. Sohnius, “All Possible Generators of Supersymmetries of the s Matrix,” *Nucl. Phys.* **B88** (1975) 257. [,257(1974)].
- [55] J. Wess and B. Zumino, “Supergauge transformations in four dimensions,” *Nuclear Physics B* **70** no. 1, (1974) 39 – 50.
<http://www.sciencedirect.com/science/article/pii/0550321374903551>.
- [56] H. Georgi and S. L. Glashow, “Gauge theories without anomalies,” *Phys. Rev. D* **6** (Jul, 1972) 429–431. <https://link.aps.org/doi/10.1103/PhysRevD.6.429>.
- [57] S. Dimopoulos and D. W. Sutter, “The Supersymmetric flavor problem,” *Nucl. Phys. B* **452** (1995) 496–512, [arXiv:hep-ph/9504415](https://arxiv.org/abs/hep-ph/9504415).
- [58] **MEG** Collaboration, T. Mori, “Final Results of the MEG Experiment,” *Nuovo Cim. C* **39** no. 4, (2017) 325, [arXiv:1606.08168 \[hep-ex\]](https://arxiv.org/abs/1606.08168).
- [59] H. P. Nilles, “Supersymmetry, Supergravity and Particle Physics,” *Phys. Rept.* **110** (1984) 1–162.
- [60] A. Lahanas and D. Nanopoulos, “The road to no-scale supergravity,” *Physics Reports* **145** no. 1, (1987) 1 – 139.
<http://www.sciencedirect.com/science/article/pii/0370157387900342>.
- [61] J. L. Feng, A. Rajaraman, and F. Takayama, “Superweakly interacting massive particles,” *Phys. Rev. Lett.* **91** (2003) 011302, [arXiv:hep-ph/0302215](https://arxiv.org/abs/hep-ph/0302215).
- [62] **Super-Kamiokande** Collaboration, K. Abe *et al.*, “Search for proton decay via $p \rightarrow e^+ \pi^0$ and $p \rightarrow \mu^+ \pi^0$ in 0.31 megaton-years exposure of the Super-Kamiokande water Cherenkov detector,” *Phys. Rev. D* **95** no. 1, (2017) 012004, [arXiv:1610.03597 \[hep-ex\]](https://arxiv.org/abs/1610.03597).
- [63] J. R. Ellis, “Beyond the standard model for hill walkers,” in *1998 European School of High-Energy Physics*, pp. 133–196. 8, 1998. [arXiv:hep-ph/9812235](https://arxiv.org/abs/hep-ph/9812235).

- [64] J. R. Ellis, J. Hagelin, D. V. Nanopoulos, K. A. Olive, and M. Srednicki, “Supersymmetric Relics from the Big Bang,” *Nucl. Phys. B* **238** (1984) 453–476.
- [65] D. O. Caldwell, R. M. Eisberg, D. M. Grumm, M. S. Witherell, B. Sadoulet, F. S. Goulding, and A. R. Smith, “Laboratory limits on galactic cold dark matter,” *Phys. Rev. Lett.* **61** (Aug, 1988) 510–513. <https://link.aps.org/doi/10.1103/PhysRevLett.61.510>.
- [66] M. Mori, M. M. Nojiri, K. S. Hirata, K. Kihara, Y. Oyama, A. Suzuki, K. Takahashi, M. Yamada, H. Takei, M. Koga, K. Miyano, H. Miyata, Y. Fukuda, T. Hayakawa, K. Inoue, T. Ishida, T. Kajita, Y. Koshio, M. Nakahata, K. Nakamura, A. Sakai, N. Sato, M. Shiozawa, J. Suzuki, Y. Suzuki, Y. Totsuka, M. Koshiba, K. Nishijima, T. Kajimura, T. Suda, A. T. Suzuki, T. Hara, Y. Nagashima, M. Takita, H. Yokoyama, A. Yoshimoto, K. Kaneyuki, Y. Takeuchi, T. Tanimori, S. Tasaka, and K. Nishikawa, “Search for neutralino dark matter heavier than the w boson at kamiokande,” *Phys. Rev. D* **48** (Dec, 1993) 5505–5518. <https://link.aps.org/doi/10.1103/PhysRevD.48.5505>.
- [67] **CDMS** Collaboration, D. S. Akerib *et al.*, “Exclusion limits on the WIMP-nucleon cross section from the first run of the Cryogenic Dark Matter Search in the Soudan Underground Laboratory,” *Phys. Rev. D* **72** (2005) 052009, [arXiv:astro-ph/0507190](https://arxiv.org/abs/astro-ph/0507190).
- [68] A. Djouadi, J.-L. Kneur, and G. Moultaka, “SuSpect: A Fortran code for the supersymmetric and Higgs particle spectrum in the MSSM,” *Comput. Phys. Commun.* **176** (2007) 426–455, [arXiv:hep-ph/0211331](https://arxiv.org/abs/hep-ph/0211331).
- [69] C. F. Berger, J. S. Gainer, J. L. Hewett, and T. G. Rizzo, “Supersymmetry without prejudice,” *Journal of High Energy Physics* **2009** no. 02, (Feb, 2009) 023–023. <http://dx.doi.org/10.1088/1126-6708/2009/02/023>.
- [70] J. Alwall, P. Schuster, and N. Toro, “Simplified Models for a First Characterization of New Physics at the LHC,” *Phys. Rev. D* **79** (2009) 075020, [arXiv:0810.3921 \[hep-ph\]](https://arxiv.org/abs/0810.3921).
- [71] **LHC New Physics Working Group** Collaboration, D. Alves, “Simplified Models for LHC New Physics Searches,” *J. Phys. G* **39** (2012) 105005, [arXiv:1105.2838 \[hep-ph\]](https://arxiv.org/abs/1105.2838).
- [72] D. S. Alves, E. Izaguirre, and J. G. Wacker, “Where the Sidewalk Ends: Jets and Missing Energy Search Strategies for the 7 TeV LHC,” *JHEP* **10** (2011) 012, [arXiv:1102.5338 \[hep-ph\]](https://arxiv.org/abs/1102.5338).
- [73] F. Ambrogi, S. Kraml, S. Kulkarni, U. Laa, A. Lessa, and W. Waltenberger, “On the coverage of the pMSSM by simplified model results,” *Eur. Phys. J. C* **78** no. 3, (2018) 215, [arXiv:1707.09036 \[hep-ph\]](https://arxiv.org/abs/1707.09036).
- [74] O. Buchmueller and J. Marrouche, “Universal mass limits on gluino and third-generation squarks in the context of Natural-like SUSY spectra,” *Int. J. Mod. Phys. A* **29** no. 06, (2014) 1450032, [arXiv:1304.2185 \[hep-ph\]](https://arxiv.org/abs/1304.2185).
- [75] **ATLAS** Collaboration, M. Aaboud *et al.*, “Dark matter interpretations of ATLAS searches for the electroweak production of supersymmetric particles in $\sqrt{s} = 8$ TeV proton-proton collisions,” *JHEP* **09** (2016) 175, [arXiv:1608.00872 \[hep-ex\]](https://arxiv.org/abs/1608.00872).
- [76] **ATLAS** Collaboration, “Summary of the ATLAS experiment’s sensitivity to supersymmetry after LHC Run 1 — interpreted in the phenomenological MSSM,” *JHEP* **10** (2015) 134, [arXiv:1508.06608 \[hep-ex\]](https://arxiv.org/abs/1508.06608).

- [77] **ATLAS** Collaboration, “Mass reach of the atlas searches for supersymmetry.” https://atlas.web.cern.ch/Atlas/GROUPS/PHYSICS/PUBNOTES/ATL-PHYS-PUB-2020-020/fig_23.png, 2020.
- [78] **CMS** Collaboration, “Summary plot moriond 2017.” https://twiki.cern.ch/twiki/pub/CMSPublic/SUSYSummary2017/Moriond2017_BarPlot.pdf, 2017.
- [79] L. S. W. Group, “Notes lepsusywg/02-04.1 and lepsusywg/01-03.1.” <http://lepsusy.web.cern.ch/lepsusy/>, 2004. Accessed: 2021-02-11.
- [80] **ATLAS** Collaboration, G. Aad *et al.*, “Observation of a new particle in the search for the Standard Model Higgs boson with the ATLAS detector at the LHC,” *Phys. Lett. B* **716** (2012) 1–29, [arXiv:1207.7214 \[hep-ex\]](https://arxiv.org/abs/1207.7214).
- [81] **CMS** Collaboration, S. Chatrchyan *et al.*, “Observation of a New Boson at a Mass of 125 GeV with the CMS Experiment at the LHC,” *Phys. Lett. B* **716** (2012) 30–61, [arXiv:1207.7235 \[hep-ex\]](https://arxiv.org/abs/1207.7235).
- [82] CERN, “About cern.” <https://home.cern/about>. Accessed: 2021-01-21.
- [83] CERN, “CERN Annual report 2019,” tech. rep., CERN, Geneva, 2020. <https://cds.cern.ch/record/2723123>.
- [84] O. S. Bruning, P. Collier, P. Lebrun, S. Myers, R. Ostojic, J. Poole, and P. Proudlock, *LHC Design Report*. CERN Yellow Reports: Monographs. CERN, Geneva, 2004. <https://cds.cern.ch/record/782076>.
- [85] M. Blewett and N. Vogt-Nilsen, “Proceedings of the 8th international conference on high-energy accelerators, cern 1971. conference held at geneva, 20–24 september 1971.,” tech. rep., 1971, 1971.
- [86] L. R. Evans and P. Bryant, “LHC Machine,” *JINST* **3** (2008) S08001. 164 p. [http://cds.cern.ch/record/1129806](https://cds.cern.ch/record/1129806). This report is an abridged version of the LHC Design Report (CERN-2004-003).
- [87] R. Scrivens, M. Kronberger, D. Küchler, J. Lettry, C. Mastrostefano, O. Midttun, M. O’Neil, H. Pereira, and C. Schmitzer, “Overview of the status and developments on primary ion sources at CERN*.”. <https://cds.cern.ch/record/1382102>.
- [88] M. Vretenar, J. Vollaire, R. Scrivens, C. Rossi, F. Roncarolo, S. Ramberger, U. Raich, B. Puccio, D. Nisbet, R. Mompo, S. Mathot, C. Martin, L. A. Lopez-Hernandez, A. Lombardi, J. Lettry, J. B. Lallement, I. Kozsar, J. Hansen, F. Gerigk, A. Funken, J. F. Fuchs, N. Dos Santos, M. Calviani, M. Buzio, O. Brunner, Y. Body, P. Baudrenghien, J. Bauche, and T. Zickler, *Linac4 design report*, vol. 6 of *CERN Yellow Reports: Monographs*. CERN, Geneva, 2020. <https://cds.cern.ch/record/2736208>.
- [89] E. Mobs, “The CERN accelerator complex - 2019. Complexe des accélérateurs du CERN - 2019.”. <https://cds.cern.ch/record/2684277>. General Photo.
- [90] **ATLAS** Collaboration, “The ATLAS Experiment at the CERN Large Hadron Collider,” *JINST* **3** (2008) S08003.
- [91] **CMS** Collaboration, S. Chatrchyan *et al.*, “The CMS Experiment at the CERN LHC,” *JINST* **3** (2008) S08004.

- [92] **ALICE** Collaboration, K. Aamodt *et al.*, “The ALICE experiment at the CERN LHC,” *JINST* **3** (2008) S08002.
- [93] **LHCb** Collaboration, J. Alves, A. Augusto *et al.*, “The LHCb Detector at the LHC,” *JINST* **3** (2008) S08005.
- [94] **TOTEM** Collaboration, G. Anelli *et al.*, “The TOTEM experiment at the CERN Large Hadron Collider,” *JINST* **3** (2008) S08007.
- [95] **LHCf** Collaboration, O. Adriani *et al.*, “Technical design report of the LHCf experiment: Measurement of photons and neutral pions in the very forward region of LHC,”.
- [96] **MoEDAL** Collaboration, J. Pinfold *et al.*, “Technical Design Report of the MoEDAL Experiment,”.
- [97] **ATLAS** Collaboration, “ATLAS Public Results - Luminosity Public Results Run 2.”. <https://twiki.cern.ch/twiki/bin/view/AtlasPublic/LuminosityPublicResultsRun2>. Accessed: 2021-01-17.
- [98] **ATLAS** Collaboration, Z. Marshall, “Simulation of Pile-up in the ATLAS Experiment,” *J. Phys. Conf. Ser.* **513** (2014) 022024.
- [99] “First beam in the LHC - accelerating science.”. <https://home.cern/news/news/accelerators/record-luminosity-well-done-lhc>. Accessed: 2021-01-10.
- [100] **ATLAS Collaboration** Collaboration, “Luminosity determination in pp collisions at $\sqrt{s} = 13$ TeV using the ATLAS detector at the LHC,” Tech. Rep. ATLAS-CONF-2019-021, CERN, Geneva, Jun, 2019. <https://cds.cern.ch/record/2677054>.
- [101] **ATLAS** Collaboration, M. Aaboud *et al.*, “Luminosity determination in pp collisions at $\sqrt{s} = 8$ TeV using the ATLAS detector at the LHC,” *Eur. Phys. J. C* **76** no. 12, (2016) 653, [arXiv:1608.03953 \[hep-ex\]](https://arxiv.org/abs/1608.03953).
- [102] G. Avoni, M. Bruschi, G. Cabras, D. Caforio, N. Dehghanian, A. Floderus, B. Giacobbe, F. Giannuzzi, F. Giorgi, P. Grafström, V. Hedberg, F. L. Manghi, S. Meneghini, J. Pinfold, E. Richards, C. Sbarra, N. S. Cesari, A. Sbrizzi, R. Soluk, G. Ucchielli, S. Valentinetti, O. Viazlo, M. Villa, C. Vittori, R. Vuillermet, and A. Zoccoli, “The new LUCID-2 detector for luminosity measurement and monitoring in ATLAS,” *Journal of Instrumentation* **13** no. 07, (Jul, 2018) P07017–P07017. <https://doi.org/10.1088/1748-0221/13/07/p07017>.
- [103] S. van der Meer, “Calibration of the effective beam height in the ISR,” Tech. Rep. CERN-ISR-PO-68-31. ISR-PO-68-31, CERN, Geneva, 1968. <https://cds.cern.ch/record/296752>.
- [104] P. Grafström and W. Kozanecki, “Luminosity determination at proton colliders,” *Progress in Particle and Nuclear Physics* **81** (2015) 97 – 148. <http://www.sciencedirect.com/science/article/pii/S0146641014000878>.
- [105] “New schedule for CERN’s accelerators and experiments.”. <https://home.cern/news/press-release/cern/first-beam-lhc-accelerating-science>. Accessed: 2021-01-10.

- [106] **ATLAS** Collaboration, G. Aad *et al.*, “Luminosity Determination in pp Collisions at $\sqrt{s} = 7$ TeV Using the ATLAS Detector at the LHC,” *Eur. Phys. J. C* **71** (2011) 1630, [arXiv:1101.2185 \[hep-ex\]](https://arxiv.org/abs/1101.2185).
- [107] **ATLAS Collaboration** Collaboration, G. Aad *et al.*, “Improved luminosity determination in pp collisions at $\sqrt{s} = 7$ TeV using the ATLAS detector at the LHC. Improved luminosity determination in pp collisions at $\text{sqrt}(s) = 7$ TeV using the ATLAS detector at the LHC,” *Eur. Phys. J. C* **73** no. CERN-PH-EP-2013-026, CERN-PH-EP-2013-026, (Feb, 2013) 2518. 27 p. <https://cds.cern.ch/record/1517411>. Comments: 26 pages plus author list (39 pages total), 17 figures, 9 tables, submitted to EPJC, All figures are available at <a href=.
- [108] “Record luminosity: well done LHC.” <https://home.cern/news/news/accelerators/new-schedule-cerns-accelerators-and-experiments>. Accessed: 2021-01-10.
- [109] A. G., B. A. I., B. O., F. P., L. M., R. L., and T. L., *High-Luminosity Large Hadron Collider (HL-LHC): Technical Design Report V. 0.1*. CERN Yellow Reports: Monographs. CERN, Geneva, 2017. <https://cds.cern.ch/record/2284929>.
- [110] J. Pequenao, “Computer generated image of the whole ATLAS detector.” Mar, 2008.
- [111] **ATLAS** Collaboration, “ATLAS: Detector and physics performance technical design report. Volume 1,” .
- [112] J. Pequenao, “Computer generated image of the ATLAS inner detector.” Mar, 2008.
- [113] **ATLAS Collaboration** Collaboration, K. Potamianos, “The upgraded Pixel detector and the commissioning of the Inner Detector tracking of the ATLAS experiment for Run-2 at the Large Hadron Collider,” Tech. Rep. ATL-PHYS-PROC-2016-104, CERN, Geneva, Aug, 2016. <https://cds.cern.ch/record/2209070>. 15 pages, EPS-HEP 2015 Proceedings.
- [114] **ATLAS IBL** Collaboration, B. Abbott *et al.*, “Production and Integration of the ATLAS Insertable B-Layer,” *JINST* **13** no. 05, (2018) T05008, [arXiv:1803.00844 \[physics.ins-det\]](https://arxiv.org/abs/1803.00844).
- [115] **ATLAS** Collaboration, “ATLAS Insertable B-Layer Technical Design Report,” Tech. Rep. CERN-LHCC-2010-013. ATLAS-TDR-19, Sep, 2010. [http://cds.cern.ch/record/1291633](https://cds.cern.ch/record/1291633).
- [116] **ATLAS** Collaboration, G. Aad *et al.*, “ATLAS b-jet identification performance and efficiency measurement with $t\bar{t}$ events in pp collisions at $\sqrt{s} = 13$ TeV,” *Eur. Phys. J. C* **79** no. 11, (2019) 970, [arXiv:1907.05120 \[hep-ex\]](https://arxiv.org/abs/1907.05120).
- [117] ATLAS Collaboration, “Particle Identification Performance of the ATLAS Transition Radiation Tracker.” ATLAS-CONF-2011-128, 2011. <https://cds.cern.ch/record/1383793>.
- [118] J. Pequenao, “Computer Generated image of the ATLAS calorimeter.” Mar, 2008.
- [119] J. Pequenao, “Computer generated image of the ATLAS Muons subsystem.” Mar, 2008.
- [120] S. Lee, M. Livan, and R. Wigmans, “Dual-Readout Calorimetry,” *Rev. Mod. Phys.* **90** no. arXiv:1712.05494. 2, (Dec, 2017) 025002. 40 p. <https://cds.cern.ch/record/2637852>. 44 pages, 53 figures, accepted for publication in Review of Modern Physics.

- [121] M. Leite, “Performance of the ATLAS Zero Degree Calorimeter,” Tech. Rep. ATL-FWD-PROC-2013-001, CERN, Geneva, Nov, 2013.
<https://cds.cern.ch/record/1628749>.
- [122] S. Abdel Khalek *et al.*, “The ALFA Roman Pot Detectors of ATLAS,” *JINST* **11** no. 11, (2016) P11013, [arXiv:1609.00249 \[physics.ins-det\]](https://arxiv.org/abs/1609.00249).
- [123] U. Amaldi, G. Cocconi, A. Diddens, R. Dobinson, J. Dorenbosch, W. Duinker, D. Gustavson, J. Meyer, K. Potter, A. Wetherell, A. Baroncelli, and C. Bosio, “The real part of the forward proton proton scattering amplitude measured at the cern intersecting storage rings,” *Physics Letters B* **66** no. 4, (1977) 390 – 394.
<http://www.sciencedirect.com/science/article/pii/0370269377900223>.
- [124] L. Adamczyk, E. Banaś, A. Brandt, M. Bruschi, S. Grinstein, J. Lange, M. Rijssenbeek, P. Sicho, R. Staszewski, T. Sykora, M. Trzebiński, J. Chwastowski, and K. Korcyl, “Technical Design Report for the ATLAS Forward Proton Detector,” Tech. Rep. CERN-LHCC-2015-009. ATLAS-TDR-024, May, 2015.
<https://cds.cern.ch/record/2017378>.
- [125] **ATLAS** Collaboration, A. R. Martínez, “The Run-2 ATLAS Trigger System,” *J. Phys. Conf. Ser.* **762** no. 1, (2016) 012003.
- [126] **ATLAS Collaboration** Collaboration, *ATLAS level-1 trigger: Technical Design Report*. Technical Design Report ATLAS. CERN, Geneva, 1998.
<https://cds.cern.ch/record/381429>.
- [127] **ATLAS** Collaboration, G. Aad *et al.*, “Operation of the ATLAS trigger system in Run 2,” *JINST* **15** no. 10, (2020) P10004, [arXiv:2007.12539 \[physics.ins-det\]](https://arxiv.org/abs/2007.12539).
- [128] **ATLAS Collaboration** Collaboration, P. Jenni, M. Nessi, M. Nordberg, and K. Smith, *ATLAS high-level trigger, data-acquisition and controls: Technical Design Report*. Technical Design Report ATLAS. CERN, Geneva, 2003.
<https://cds.cern.ch/record/616089>.
- [129] **ATLAS** Collaboration, G. Aad *et al.*, “The ATLAS Simulation Infrastructure,” *Eur. Phys. J. C* **70** (2010) 823–874, [arXiv:1005.4568 \[physics.ins-det\]](https://arxiv.org/abs/1005.4568).
- [130] T. Gleisberg, S. Hoeche, F. Krauss, M. Schonherr, S. Schumann, F. Siegert, and J. Winter, “Event generation with SHERPA 1.1,” *JHEP* **02** (2009) 007, [arXiv:0811.4622 \[hep-ph\]](https://arxiv.org/abs/0811.4622).
- [131] A. Buckley *et al.*, “General-purpose event generators for LHC physics,” *Phys. Rept.* **504** (2011) 145–233, [arXiv:1101.2599 \[hep-ph\]](https://arxiv.org/abs/1101.2599).
- [132] V. N. Gribov and L. N. Lipatov, “Deep inelastic e p scattering in perturbation theory,” *Sov. J. Nucl. Phys.* **15** (1972) 438–450.
- [133] J. Blumlein, T. Doyle, F. Hautmann, M. Klein, and A. Vogt, “Structure functions in deep inelastic scattering at HERA,” in *Workshop on Future Physics at HERA (To be followed by meetings 7-9 Feb and 30-31 May 1996 at DESY)*. 9, 1996. [arXiv:hep-ph/9609425](https://arxiv.org/abs/hep-ph/9609425).
- [134] A. Buckley, J. Ferrando, S. Lloyd, K. Nordström, B. Page, M. Rüfenacht, M. Schönherr, and G. Watt, “LHAPDF6: parton density access in the LHC precision era,” *Eur. Phys. J. C* **75** (2015) 132, [arXiv:1412.7420 \[hep-ph\]](https://arxiv.org/abs/1412.7420).

- [135] M. Bengtsson and T. Sjostrand, “Coherent Parton Showers Versus Matrix Elements: Implications of PETRA - PEP Data,” *Phys. Lett. B* **185** (1987) 435.
- [136] S. Catani, F. Krauss, R. Kuhn, and B. R. Webber, “QCD matrix elements + parton showers,” *JHEP* **11** (2001) 063, [arXiv:hep-ph/0109231](https://arxiv.org/abs/hep-ph/0109231).
- [137] L. Lonnblad, “Correcting the color dipole cascade model with fixed order matrix elements,” *JHEP* **05** (2002) 046, [arXiv:hep-ph/0112284](https://arxiv.org/abs/hep-ph/0112284).
- [138] B. Andersson, G. Gustafson, G. Ingelman, and T. Sjostrand, “Parton Fragmentation and String Dynamics,” *Phys. Rept.* **97** (1983) 31–145.
- [139] B. Andersson, *The Lund Model*. Cambridge Monographs on Particle Physics, Nuclear Physics and Cosmology. Cambridge University Press, 1998.
- [140] D. Amati and G. Veneziano, “Preconfinement as a Property of Perturbative QCD,” *Phys. Lett. B* **83** (1979) 87–92.
- [141] D. Yennie, S. Frautschi, and H. Suura, “The infrared divergence phenomena and high-energy processes,” *Annals of Physics* **13** no. 3, (1961) 379–452.
<https://www.sciencedirect.com/science/article/pii/0003491661901518>.
- [142] M. Dobbs and J. B. Hansen, “The HepMC C++ Monte Carlo event record for High Energy Physics,” *Comput. Phys. Commun.* **134** (2001) 41–46.
- [143] **GEANT4** Collaboration, S. Agostinelli *et al.*, “GEANT4: A Simulation toolkit,” *Nucl. Instrum. Meth. A* **506** (2003) 250–303.
- [144] **ATLAS Collaboration** Collaboration, “The new Fast Calorimeter Simulation in ATLAS,” Tech. Rep. ATL-SOFT-PUB-2018-002, CERN, Geneva, Jul, 2018.
<https://cds.cern.ch/record/2630434>.
- [145] K. Cranmer, “Practical Statistics for the LHC,” in *2011 European School of High-Energy Physics*, pp. 267–308. 2014. [arXiv:1503.07622 \[physics.data-an\]](https://arxiv.org/abs/1503.07622).
- [146] G. Cowan, K. Cranmer, E. Gross, and O. Vitells, “Asymptotic formulae for likelihood-based tests of new physics,” *Eur. Phys. J. C* **71** (2011) 1554,
[arXiv:1007.1727 \[physics.data-an\]](https://arxiv.org/abs/1007.1727). [Erratum: Eur. Phys. J.C73,2501(2013)].
- [147] ATLAS Collaboration, “Reproduction searches for new physics with the ATLAS experiment through publication of full statistical likelihoods.” ATL-PHYS-PUB-2019-029, 2019. <https://cds.cern.ch/record/2684863>.
- [148] **ROOT Collaboration** Collaboration, K. Cranmer, G. Lewis, L. Moneta, A. Shibata, and W. Verkerke, “HistFactory: A tool for creating statistical models for use with RooFit and RooStats,” Tech. Rep. CERN-OPEN-2012-016, New York U., New York, Jan, 2012.
<https://cds.cern.ch/record/1456844>.
- [149] W. Verkerke and D. P. Kirkby, “The RooFit toolkit for data modeling,” *eConf C0303241* (2003) MOLT007, [arXiv:physics/0306116 \[physics\]](https://arxiv.org/abs/physics/0306116). [,186(2003)].
- [150] L. Moneta, K. Belasco, K. S. Cranmer, S. Kreiss, A. Lazzaro, D. Piparo, G. Schott, W. Verkerke, and M. Wolf, “The RooStats Project,” *PoS ACAT2010* (2010) 057,
[arXiv:1009.1003 \[physics.data-an\]](https://arxiv.org/abs/1009.1003).